Diffraction Analysis of Slanted-Finger Interdigital Transducers

Guenter Martin and Dongpei Chen, *Member, IEEE*

***Abstract*—For analysis, slanted-finger interdigital transducers (SFITs) are usually divided into many channels in parallel to the propagation direction. Every channel is considered to be a subfilter. This procedure neglects the diffraction completely. This paper introduces the diffraction in the SFIT analysis by use of the angular spectrum of plane waves (ASPW) approach. The analysis is based on a one-component bulk-wave model. The integrals of an ASPW are carried out by summing up M wave components with various wave vectors. Two wave modes propagating toward both forward and backward directions within SFIT are assumed to take the coupling effect into account. The amplitudes of both wave modes are expressed by M-dimensional vectors. By means of the boundary conditions at every finger edge, the transfer matrix and transduction vector are found. As a result, coupling-of-modes-like equations that link wave components at adjacent finger and gap regions are obtained. Those wave vectors are generally inclined with respect to each other. As a consequence, the transfer matrix, for instance, of any finger and that of the total SFIT are $2M \times 2M$ matrices. By matrix–matrix and matrix–vector multiplication, the complex amplitudes of all the wave components in all the finger and gap regions are calculated. These amplitudes yield the total wave field including reflection at all fingers. The wave field yields the piezoelectric part of the input and output transducer currents as functions of the filter input and output voltages representing the piezoelectric part of the Y matrix. The model is used for analyzing a unidirectional SFIT filter, the transducers of which are composed of SPUDT cells on 37° YX quartz. The simulated transmission behavior is compared with experimental results. Good agreement is found. Especially for the case of a large slanted angle, the profound deformation appearing within the passband and the high-frequency transition band can be clearly identified as the most important influence of the diffraction on the transmission behavior.**

***Index Terms*—Diffraction analysis, SAW transducers, slanted electrodes, unidirectional SFIT filter.**

I. Introduction

SLANTED-FINGER interdigital transducers (SFITs) were first suggested by van den Heuvel in 1972 [1]. Instead of SFITs, other expressions, such as a tapered transducer or fan-shaped transducer are also used. All the SFIT structures are characterized by finger arrangements like a divergent bundle. Later, in particular, in the 1990s, SFITs became important for wide-band filters with flat passband, steep skirts, and good stopband rejection [2]–[11]. Saw and Campbell [9], as well as Solie [10] suggested to combine tapered electrode structures and single-phase interdigital transducer (SPUDT) cells. As a consequence, reflectionless SFITs are feasible, in particular, by weighting the cell reflection coefficient. From [12], it is known that a SPUDT can be made reflectionless in a favorable manner when the reflection weighting function is the self-convolution of the transduction weighting function. Now, this can also be applied to SFITs. The triple transit echo is negligible. SPUDTs are applicable for narrow-band low-loss filters. Now, however, according to [9] and [10], wide-band low-loss filters can be realized. In this paper, such transducers are called unidirectional slanted-finger interdigital transducers (USFITs). To meet filter specifications, transduction weighting is required as a rule. Some weighting methods were investigated, for instance, withdrawal weighting [5], [6] and series block weighting [10], [11], which is sometimes called capacitive weighting.

For analysis usually used (for instance, [4]–[11]), SFITs are divided into many channels in parallel to the propagation direction. Every channel is considered to be a subfilter to be independent of the other subfilters. This procedure neglects the diffraction completely. As an influence of the diffraction, interaction of subfilters must be expected. Chvets *et al.* [11] studied the influence of the diffraction on the transmission behavior of an SFIT filter experimentally by varying the transducer aperture. Measurements showed that, for small apertures, some deviation from predictions in the passband and upper transition band exist, and are likely caused by neglecting diffraction effects.

The purpose of this paper is to propose an analysis method for SFIT filters taking diffraction into account. For this, the angular spectrum of plane waves (ASPW) approach is used. This approach uses the general solution of the linear wave equation. According to [14], this solution is an integral over plane-wave components with k_y as an integration variable, as shown in the following:

$$\int_{-\infty}^{\infty} dk_y \psi(k_y) \exp\left[i(xk_x(k_y)+yk_y)\right], \qquad k_y = k(\beta)\sin\beta. \tag{1}$$

The angle β is the tilt angle of the wave vector of the respective plane-wave component with respect to the x-axis and $k(\beta)$ is the angle-dependent wave vector. The integral boundaries $\pm\infty$ in (1) are an approximation. The function $\psi(k_y)$ can be calculated from the initial state $u(0, y)$ of the wave field by Fourier transformation. If $\psi(k_y)$ and $k(\beta)$ are known, the wave field $u(x, y)$ can be calculated by means of (1).

II. Scattering of an Angular Spectrum of Plane Waves at a Slanted-Finger Edge

Fig. 1 schematically shows the transducer structure of an SFIT filter.

Manuscript received October 9, 2000; revised January 9, 2001.

G. Martin is with the Institute for Solid State and Materials Research Dresden, D-01171 Dresden, Germany.

D. Chen is with Vectron International, Hudson, NH 03051 USA.

Publisher Item Identifier S 0018-9480(01)02911-8.

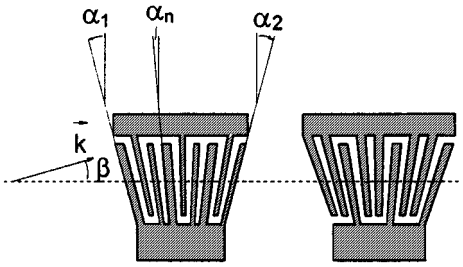

Fig. 1. Sketch of an SFIT filter.

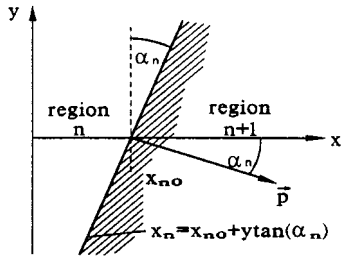

Fig. 2. Geometric characterization of an electrode edge (n = tilt angle, $\vec{p}$ = edge normal vector).

By means of Fig. 1, we want to explain some important angle definitions, which are necessary for analysis. The range of the electrode edge tilt angle is defined, for instance, for the left SFIT as follows:

$$\alpha_1 \leq \alpha_n \leq \alpha_{2N}. \tag{2}$$

N is the total finger number per SFIT. In Fig. 1, α_{2N} is denoted by α_2. α_n is the tilt angle of the nth electrode edge. It is defined as a positive angle when tilt is clockwise, but as a negative one when tilt is counterclockwise. β is the angle that is formed by the component of the ASPW with the wave vector $\vec{k}$, with the main propagation direction visualized by a dashed line in Fig. 1.

Let us now discuss the scattering of waves that can be characterized by an ASPW. To do this, Fig. 2 shows that a slanted electrode edge is used. This edge separates a free and a metallized region n and $n+1$, respectively. It is a straight line and is described by the following:

$$x_n = x_{n0} + y\tan(\alpha_n). \tag{3}$$

The vector $\vec{p}$ is the normal vector of the edge. The one-component model from [13] is used for analysis. It is similar to the crossed-field model, but it does not apply equivalent circuits for characterizing electrodes or transducer periods. That model yields a wave equation for one particle displacement $\tilde{u}_n$ of every plane-wave component within the nth region of

$$\frac{\partial^2 \tilde{u}_n}{\partial t^2} - v_n(\beta)\frac{\partial^2 \tilde{u}_n}{\partial x'^2} = 0$$
$$\frac{\partial^2 \tilde{u}_n}{\partial x'^2} = \left(\frac{\partial^2}{\partial x^2} + \frac{\partial^2}{\partial y^2}\right)\tilde{u}_n$$
$$x' = x\cos(\beta) + y\sin(\beta) \tag{4a}$$

where x' is the x coordinate along the propagation direction that is slanted by the angle β with respect to the main propagation direction. According to the model considered, there is only one elastic stiffness c and one piezoelectric constant e, which can be denoted as an effective piezoelectric constant. They are attributed to the known surface acoustic wave (SAW) parameters' velocity $v(\beta)$, coupling coefficient $K^2(\beta)$, and capacity/(finger pair $\times$ aperture) $C_p(\beta)$ by

$$c(\beta) = \rho v^2(\beta) \quad e(\beta) = \sqrt{\rho v^2(\beta) K^2(\beta) C_p(\beta)}. \tag{4b}$$

$c(\beta)$ in the region n is called $c_n(\beta)$. One can show that, in the case of slanted propagating plane waves, the derivatives to x for x-propagating plane waves can replaced by derivatives to x' from (4a). This remark will also be important for determining the dielectric displacement in (20). To the first-order approximation, the dependence of e on the region number is so weak that it can be ignored. The density ρ is assumed to be constant. We want to form an expression for the superposition of the solutions of (4a) for all the possible propagation directions. Such an expression is given in (5). The following represents a solution according to (1), which includes plane-wave components into all directions:

$$u_n(x,y) = \int_{-\pi/2-\alpha_n}^{\pi/2-\alpha_n} d\beta_n^R R_n(\beta_n^R) \cdot \exp\left[ik_n(-x\cos(\beta_n^R) + y\sin\left(\beta_n^R\right))\right] + \int_{-\pi/2+\alpha_n}^{\pi/2+\alpha_n} d\beta_n^S S_n(\beta_n^S) \cdot \exp\left[ik_n(x\cos(\beta_n^S) + y\sin\left(\beta_n^S\right))\right]. \tag{5}$$

R_n and S_n are complex amplitudes of the plane-wave components in the region n that are incident to the edge x_n from region n and are radiated from this edge to region n, respectively. Particle displacement u and mechanical stress T have to be continuous at the electrode edges. Therefore, the following boundary conditions must be met:

$$u_{n+1}(x_n, y) - u_n(x_n, y) = 0 \tag{6a}$$
$$T_{n+1}(x_n, y) - T_n(x_n, y) = 0. \tag{6b}$$

If the region n and $n+1$ is a gap and electrode region, the electric crossed field E_n is zero and E_{n+1} is nonzero, respectively. Therefore, the mechanical stress is given by

$$T_n = c_n\frac{\partial u_n}{\partial x'} \quad T_{n+1} = c_{n+1}\frac{\partial u_{n+1}}{\partial x'} - eE_{n+1} \tag{6c}$$

with x' is from (3). T_n and T_{n+1} in (6b) mean the mechanical stress acting on the area that is defined by the edge and direction perpendicular to the electrode area. The mechanical stress of the model wave acts on that area for which the wave vector is the normal. Therefore, the continuity of mechanical stress can be attributed to an equation including direction derivatives of the type $\partial u/\partial p$ with respect to the normal vector $\vec{p}$ of the edge. According to our model, one obtains

$$c_{n+1}\frac{\partial u_{n+1}}{\partial p} - e(\alpha_n)E_{n+1}(y) - c_n\frac{\partial u_n}{\partial p} = 0$$
$$\frac{\partial u}{\partial p} = \vec{p}\,\mathrm{grad}(u)$$
$$\vec{p}_n = \left(\cos(\alpha_n), \sin\left(\alpha_n\right)\right) \tag{6d}$$

from (6b). Due to the limited aperture of the electrodes, the electric field has a profile in y-direction expressed by

$$E_{n+1}(y) = \begin{cases} E^0_{n+1}, & \text{if } -\dfrac{B}{2} \le y \le \dfrac{B}{2} \\ 0, & \text{otherwise} \end{cases} \quad B = \text{aperture.} \tag{6e}$$

According to our assumption, the region $n+1$ is solely metallized. Therefore, for the electric crossed fields, $E_{n+1} \neq 0$ and $E_n = 0$ are valid. $E_{n+1}(y)$ is the profile of the excitation field perpendicular to the main propagation direction. By inserting (5) into (6a) and using (3), one finds

$$\begin{aligned}
&\int_{-\pi/2-\alpha_n}^{\pi/2-\alpha_n} d\beta^R_{n+1}\, R(\beta^R_{n+1}) \\
&\quad \cdot \exp\left[-ik_{n+1}\left(x_{n0}\cos\left(\beta^R_{n+1}\right) + y\left(\frac{\sin\left(\alpha_n - \beta^R_{n+1}\right)}{\cos(\alpha_n)}\right)\right)\right] \\
&\quad + \int_{-\pi/2+\alpha_n}^{\pi/2+\alpha_n} d\beta^S_{n+1}\, S\left(\beta^S_{n+1}\right) \\
&\quad \cdot \exp\left[ik_{n+1}\left(x_{n0}\cos\left(\beta^S_{n+1}\right) + y\left(\frac{\sin\left(\alpha_n + \beta^S_{n+1}\right)}{\cos(\alpha_n)}\right)\right)\right] \\
&\quad - \left\{\int_{-\pi/2-\alpha_n}^{\pi/2-\alpha_n} d\beta^R_n\, R(\beta^R_n)\right. \\
&\qquad \cdot \exp\left[-ik_n\left(x_{n0}\cos\left(\beta^R_n\right) + y\left(\frac{\sin\left(\alpha_n - \beta^R_n\right)}{\cos(\alpha_n)}\right)\right)\right] \\
&\qquad + \int_{-\pi/2+\alpha_n}^{\pi/2+\alpha_n} d\beta^S_n\, S\left(\beta^S_n\right) \\
&\qquad \left.\cdot \exp\left[ik_n\left(x_{n0}\cos\left(\beta^S_n\right) + y\left(\frac{\sin\left(\alpha_n + \beta^S_n\right)}{\cos(\alpha_n)}\right)\right)\right]\right\} \\
&= 0.
\end{aligned} \tag{7}$$

Equation (7) can be held for all y values only if all the factors of the type $\exp[ky(\sin(\alpha \pm \beta)/\cos(\alpha)]$ in (7) are equal (phase matching). As a result, the following relationships are obtained:

$$\beta^S_n = \beta^R_n - 2\alpha_n \tag{8a}$$

$$\beta^S_{n+1} = \beta^R_{n+1} - 2\alpha_n \tag{8a}$$

$$\frac{\sin(\alpha_n - \beta^R_{n+1})}{\sin(\alpha_n - \beta^R_n)} = \frac{k_n}{k_{n+1}}. \tag{8b}$$

Equations (8a) and (8b) represent the known reflection and refraction law, respectively. They offer connections between the angles β^R_{n+1}, β^R_n, β^S_{n+1}, and β^S_n. Consequently, the integrals in (7) can be attributed to only one. The exponential function including y can be written as a factor of the integrand, as shown by the following:

$$\begin{aligned}
&\int_{-\pi/2-\alpha_n}^{\pi/2-\alpha_n} d\beta \left\{ R_{n+1}\left(\beta^R_{n+1}\right)\exp(-ik_{n+1,x}x_{n0}) \right. \\
&\qquad + S_{n+1}\left(\beta^R_{n+1} - 2\alpha_n\right)\exp(ik_{n+1,x}x_{n0}) \\
&\qquad - \left[R_n(\beta)\exp(-ik_{n,x}x_{n0}) + S_n(\beta - 2\alpha_n)\right. \\
&\qquad \left.\left. \cdot \exp(ik_{n,x}x_{n0})\right]\right\} \\
&\cdot \exp\left[-ik_n y\left(\frac{\sin(\alpha_n - \beta)}{\cos(\alpha_n)}\right)\right] = 0, \qquad \beta = \beta^R_n; \\
&k_{n+1,x} = k_{n+1}\cos(\beta^R_{n+1}); \quad k_{n,x} = k_n\cos(\beta).
\end{aligned} \tag{9}$$

In an analogous manner, one obtains

$$\begin{aligned}
&\int_{-\pi/2-\alpha_n}^{\pi/2-\alpha_n} d\beta\, ik_{n+1}c_{n+1} \\
&\cdot \left\{-\cos\left(\alpha_n + \beta^R_{n+1}\right)R_{n+1}\left(\beta^R_{n+1}\right)\exp(-ik_{n+1,x}x_{n0})\right. \\
&\quad + \cos\left(3\alpha_n - \beta^R_{n+1}\right)S_{n+1}\left(\beta^R_{n+1} - 2\alpha_n\right)\exp(ik_{n+1,x}x_{n0}) \\
&\quad - \frac{z_n}{z_{n+1}}\left[-\cos\left(\alpha_n + \beta\right)R_n(\beta)\exp(-ik_{n,x}x_{n0})\right. \\
&\qquad \left.\left. + \cos(3\alpha_n - \beta)S_n(\beta - 2\alpha_n)\exp(ik_{n,x}x_{n0})\right]\right\} \\
&\cdot \exp\left[-ik_n y\left(\frac{\sin(\alpha_n - \beta}{\cos(\alpha_n)}\right)\right] = eE_{n+1}(y), \\
&z_n = k_n c_n = \omega\rho_n v_n
\end{aligned} \tag{10}$$

by inserting (5) into (6d). When c_n and c_{n+1} are assumed to be functions of β, they must be written as parts of the integrand. In (9) and (10), β^R_{n+1} can be attributed to β by means of (8b).

Now, we have to solve the problem to deduce equations that connect R_{n+1} and S_{n+1} with R_n and S_n. Again, the integral in (9) could keep being zero for all values of y only if its integrand is zero, and then it results in the following:

$$\begin{aligned}
&R_{n+1}\left(\beta^R_{n+1}\right)\exp(-ik_{n+1,x}x_{n0}) \\
&\quad + S_{n+1}\left(\beta^R_{n+1} - 2\alpha_n\right)\exp(ik_{n+1,x}x_{n0}) \\
&\quad - \left[R_n(\beta)\exp(-ik_{n,x}x_{n0})\right. \\
&\qquad \left. + S_n\left(\beta - 2\alpha_n\right)\exp(ik_{n,x}x_{n0})\right] = 0.
\end{aligned} \tag{11}$$

The integrand of the integral from (10) is gained by Fourier transformation of the excitation field profile from (6e). We obtain

$$\begin{aligned}
&-\cos\left(\alpha_n + \beta^R_{n+1}\right)R_{n+1}\left(\beta^R_{n+1}\right)\exp(-ik_{n+1,x}x_{n0}) \\
&+\cos\left(3\alpha_n - \beta^R_{n+1}\right)S_{n+1}\left(\beta^R_{n+1} - 2\alpha_n\right) \\
&\cdot \exp(ik_{n+1,x}x_{n0}) \\
&- \frac{z_n}{z_{n+1}}\left[-\cos(\alpha_n + \beta)R_n(\beta)\exp(-ik_{n,x}x_{n0})\right. \\
&\qquad \left. + \cos(3\alpha_n - \beta)S_n(\beta - 2\alpha_n)\exp(ik_{n,x}x_{n0})\right] \\
&= \frac{eE^0_{n+1}}{ik_{n+1}c_{n+1}}\,\frac{k_n}{2\pi\cos(\alpha_n)}\int_{-B/2}^{B/2} dy \\
&\cdot \exp\left[-ik_n y\left(\frac{\sin\left(\alpha_n - \beta\right)}{\cos(\alpha_n)}\right)\right].
\end{aligned} \tag{12}$$

III. Wave Field of an SFIT

From (12), equations of the type

$$\begin{aligned} R_{n+1}(\beta_{n+1}^R) &= b_{11}(\beta,\alpha_n)R_n(\beta)+b_{12}(\beta,\alpha_n) \\ &\quad\cdot S_n(\beta-2\alpha_n)-\frac{eE_{n+1}^0}{ik_{n+1}c_{n+1}}q_1(\beta,\alpha_n) \\ S_{n+1}(\beta_{n+1}^R-2\alpha_n) &= b_{21}(\beta,\alpha_n)R_n(\beta)+b_{22}(\beta,\alpha_n) \\ &\quad\cdot S_n(\beta-2\alpha_n)-\frac{eE_{n+1}^0}{ik_{n+1}c_{n+1}}q_2(\beta,\alpha_n) \end{aligned} \tag{13}$$

that R_{n+1} and S_{n+1} attribute to R_n, S_n, and to the excitation field can be derived. The elements of the transfer matrix b_{ij} and transduction vector q_i are summarized in the following:

$$\begin{aligned} b_{11} &= \frac{1}{D}\Big[\cos(3\alpha_n-\beta_{n+1}^R)+(z_n/z_{n+1})\cos(\alpha_n+\beta)\Big] \\ &\quad\cdot\exp\Big[i(k_{n+1,x}-k_{n,x})x_{n0}\Big] \\ b_{12} &= \frac{1}{D}\Big[\cos(3\alpha_n-\beta_{n+1}^R)-(z_n/z_{n+1})\cos(3\alpha_n-\beta)\Big] \\ &\quad\cdot\exp\Big[i(k_{n+1,x}+k_{n,x})x_{n0}\Big] \\ b_{21} &= \frac{1}{D}\Big[\cos(\alpha_n+\beta_{n+1}^R)-(z_n/z_{n+1})\cos(\alpha_n+\beta)\Big] \\ &\quad\cdot\exp\Big[-i(k_{n+1,x}+k_{n,x})x_{n0}\Big] \\ b_{22} &= \frac{1}{D}\Big[\cos(\alpha_n+\beta_{n+1}^R)+(z_n/z_{n+1})\cos(3\alpha_n-\beta)\Big] \\ &\quad\cdot\exp\Big[-i(k_{n+1,x}-k_{n,x})x_{n0}\Big] \\ q_1 &= F\exp(ik_{n+1,x}x_{n0}) \\ q_2 &= -F\exp(-ik_{n+1,x}x_{n0}) \\ F &= \left(\frac{k_nB}{2\pi D}\right) \\ &\quad\cdot\frac{\sin\Big[k_nB\sin(\alpha_n-\beta)/2\cos(\alpha_n)\Big]}{k_nB\sin(\alpha_n-\beta)/2} \\ D &= \cos(3\alpha_n-\beta_{n+1}^R)+\cos(\alpha_n+\beta_{n+1}^R). \end{aligned} \tag{14}$$

To calculate the wave field numerically, the continuum of the angle β is replaced by discrete β elements. As far as the computing time is concerned, the β range is actually limited to $\beta_1 \le \beta \le \beta_2$. Moreover, we choose a suitable number M of elements. The convergence behavior for increasing the β range and increasing the element number must be checked. Every β element is characterized by a number m, which is given by

$$m = 1+\text{round}\left(\frac{\beta-\beta_1}{\delta\beta}\right), \qquad 1\le m\le M; \quad \delta\beta=\frac{\beta_2-\beta_1}{M-1}. \tag{15}$$

As a result, the equations in (13) change into

$$\begin{aligned} R_{n+1}^{\mu} &= b_{11,n}^{\mu,m}R_n^m + b_{12,n}^{\mu,m}S_n^{p(m)} - \frac{eE_{n+1}^0}{ik_{n+1}c_{n+1}}q_{1,n}^m \\ S_{n+1}^{\lambda} &= b_{21,n}^{\lambda,m}R_n^m + b_{22,n}^{\lambda,m}S_n^{p(m)} - \frac{eE_{n+1}^0}{ik_{n+1}c_{n+1}}q_{2,n}^m \\ \mu &= 1+\text{round}\Big[(\beta_{n+1}^R-\beta_1)/\delta\beta\Big] \end{aligned}$$

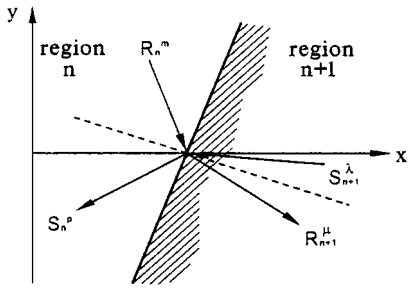

Fig. 3. Wave scattering at an electrode edge, visualization of reflected and transmitted (refracted) amplitudes.

$$\begin{aligned} \lambda &= 1+\text{round}\Big[(\beta_{n+1}^R-2\alpha_n-\beta_1)/\delta\beta\Big] \\ p(m) &= 1+\text{round}\Big[(\beta-2\alpha_n-\beta_1)/\delta\beta\Big]. \end{aligned} \tag{16}$$

For the numbers μ, λ, and p in (16), the same range is valid like m in (15). By (16), wave components with different numbers in general, i.e., different directions, in adjacent regions are linked with each other. Only in the case of $\alpha_n = 0$ are all the propagation directions are equal or opposite. In Fig. 3, the R and S vectors in (16) are explained by means of an example. In every region $(n, n+1, \ldots)$, the R and S vectors can be combined to one $2M$-dimensional vector. As a result, the combined b matrices form a $2M \times 2M$ matrix. As known, this reduces to a 2×2 matrix when only one plane-wave component is taken into account.

The calculation of the SFIT wave field is based on (16). It is carried out in the following steps.

Step 1) The transfer matrix and transduction vector of an electrode (finger) is calculated by matrix–matrix and matrix–vector multiplication.

Step 2) By means of matrix–matrix and matrix–vector multiplication of the transfer matrices and electrode transduction vectors, all the R and S amplitudes inside the SFIT are attributed to those outside the SFIT. They are called R_{left}^m, S_{left}^m, R_{right}^m, and S_{right}^m and are visualized in Fig. 4.

As a result, a equation system of the type

$$\begin{aligned} R_{\text{right}}^m &= \sum_{\mu=1}^{M} d_{11}^{m,\mu}R_{\text{left}}^{\mu} + \sum_{\mu=1}^{M} d_{12}^{m,\mu}S_{\text{left}}^{\mu} + t_{1,m}U_{\text{IDT}} \\ S_{\text{right}}^m &= \sum_{\mu=1}^{M} d_{22}^{m,\mu}S_{\text{left}}^{\mu} + \sum_{\mu=1}^{M} d_{21}^{m,\mu}R_{\text{left}}^{\mu} + t_{2,m}U_{\text{IDT}} \end{aligned} \tag{17}$$

is obtained, where $d_{ij}^{m,\mu}$ and $t_{i,m}$ are the elements of the transfer matrix and transduction vector, respectively. The transducer voltage is called U_{IDT}. No waves are assumed to be incident to the transducer. Consequently,

$$R_{\text{left}}^m = 0 \quad S_{\text{right}}^m = 0 \tag{18}$$

is valid. By inserting (18) into (17), a linear equation system for S_{left}^m is found, which is represented by the following:

$$\sum_{\mu=1}^{M} d_{22}^{m,\mu}S_{\text{left}}^{\mu} + t_{2,m}U_{\text{IDT}} = 0. \tag{19}$$

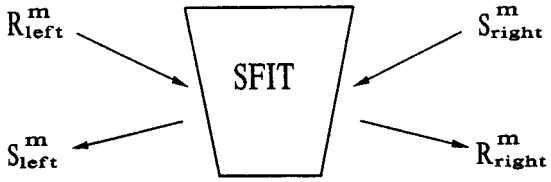

Fig. 4. Wave amplitudes outside an SFIT.

The determination of S^m_{left} as a function of U_{IDT} is the basis for calculating the R and S vectors in all the transducer electrodes and gaps according to (16). Afterwards, the wave field can be calculated in the entire transducer by means of (5).

From the wave field u_n in the nth region, the only dielectric displacement component D_n, which exists according to the model, can be calculated as follows:

$$D_n(x,y,\beta,U_{\text{IDT}}) = e(\beta)\frac{\partial \tilde{u}_n(x,y,\beta,U_{\text{IDT}})}{\partial x'} + \varepsilon_0 \varepsilon^S E_n. \tag{20}$$

We suppose that the region with the number n is an electrode region. The current I_n through the concerning electrode is given by integration of D_n over x, y, as shown in the following:

$$I_n(U_{\text{IDT}}) = i\omega \int_{-\pi/2-\alpha_n}^{\pi/2-\alpha_n} \frac{d\beta}{\pi} \cdot \iint\limits_{\substack{\text{electrode}\\ \text{area}}} dx\,dy\, s_n D_n(x,y,\beta,U_{\text{IDT}}) \tag{21}$$

(s_n = electrode polarity). The total current through the transducer under consideration is obtained by summing up contributions of all the single electrodes. The total current is a linear function of U_{IDT}. This function yields the transducer admittance.

Of course, the treatment shown here for a one-port device can be generalized for two-port devices. As a result, input and output currents are obtained as functions of the input and output voltages, thereby yielding the Y matrix.

The foregoing analysis allows to include slanted electrodes. On the other hand, electrode tilt is not necessary because the tilt angle α_n may set to zero for all electrode edges. Therefore, the analysis described is also applicable to an interdigital transducer (IDT) with withdrawal weighted parallel electrodes, for instance, an SPUDT.

IV. Filter Example

In order to test the capability of the analysis described here, a filter consisting of two identical USFITs on 37^0 YX quartz was investigated. Distributed acoustic reflection transducer (DART) cells were used to implement the unidirectional effect. The structure parameters are listed in Table I. The measured result for $|S_{21}|$ on 50 Ω is shown in Fig. 5. For comparison, the analyzed $|S_{21}|$ curve is depicted in Fig. 6(a) (solid curve). The anisotropy of the propagation velocity v is taken into account as a parabolic approximation according to the following:

$$v(\beta) = v_0\left(1 + \frac{\gamma}{2}\beta^2\right). \tag{22}$$

TABLE I
Structure Parameters of the Test Filter

Parameter	Value
Substrate	37^0 YX quartz
Number of DART cells per SFIT	120
Spacer between SFIT (μm)	186.27
Tilt angle range (degree)	- 6.0 … 6.0
Aperture (μm)	643 = 36 mean wavelengths
Minimum wavelength (μm)	17.28
Maximum wavelength (μm)	18.40
Transduction weighting	uniform (unweighted)
Reflection weighting	uniform (unweighted)
Al layer thickness (nm)	92.5

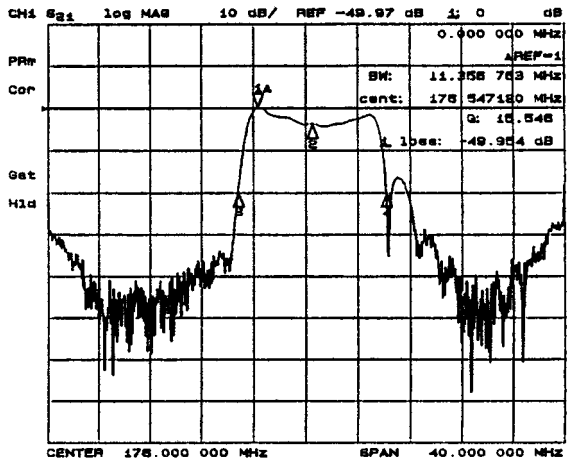

Fig. 5. Measured $|S_{21}|$ for an SFIT filter, the parameters of which are summarized in Table I.

According to Fig. 1, β is the angle that is formed by the wave vector of the considered plane-wave component and the main propagation direction (dashed line in Fig. 1). The velocity in this direction is called v_0. In Fig. 6(a), a solid curve, i.e., $\gamma = 0.35$, was used. The dashed curve in Fig. 6(a) represents the same filter without diffraction. This case was simulated by $\gamma = -1$ (ideal self-focusing). That is the reason for the essentially smaller insertion loss. By comparing both curves in Fig. 6(a), we find that the diffraction generates a dip in the passband and a strong ripple at the high-frequency transition band and in the near upper stopband. The features are also found experimentally. γ is actually not known inside the finger region of the SFIT. Therefore, $|S_{21}|$ was calculated for $\gamma = 0.3$, 0.4, and 0.5. The result is given in Fig. 6(b). The differences within the passband are not so important, but differences are clearer in the upper stopband. The best agreement seems to be present between $\gamma = 0.3$ and 0.4. Therefore, $\gamma = 0.35$ was chosen for the simulation in Fig. 6(a).

The suitability of the presented analysis method for SFIT filters is expressed by the good agreement of simulation and experiment.

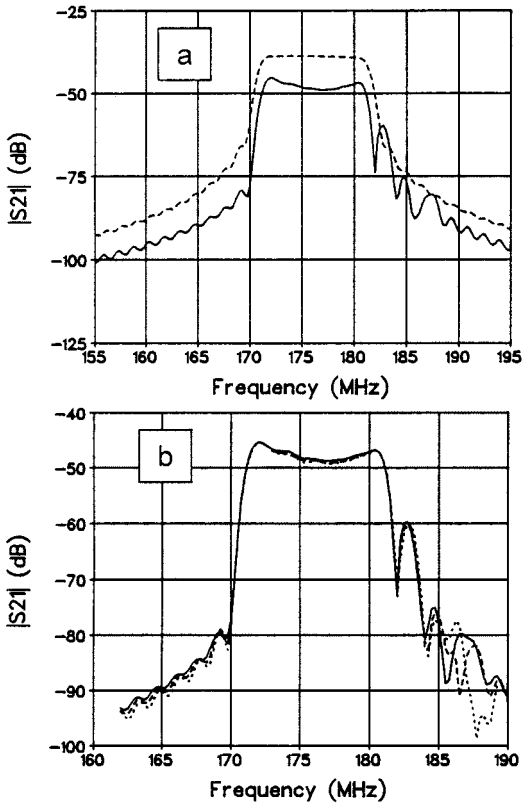

Fig. 6. Simulated $|S_{21}|$ of the filter from Table I. (a) Solid line: $\gamma = 0.35$, dashed line: $\gamma = -1$ (self-focusing case). (b) Solid line: $\gamma = 0.30$, dashed line: $\gamma = 0.40$, dotted line: $\gamma = 0.50$.

V. Summary and Conclusions

The effect of diffraction on the transmission behavior of SFITs has been described in this paper. An analysis method for SFIT including diffraction that is based on the ASPW approach has also been presented, which comprises the following steps.

- Step 1) Generalize one-component model from [13] for plane waves for slanted wave vectors.
- Step 2) Scattering of plane waves at a slanted electrode edge.
- Step 3) Describe reflection, refraction, and excitation at a slanted electrode edge with finite aperture.
- Step 4) Change from continuous angular spectrum to finite angle elements.
- Step 5) Calculate plane-wave amplitudes as functions of transducer voltage.
- Step 6) Calculate the transducer current as a function of transducer voltage resulting in admittance (Y) matrix.

Simulated and experimental results of $|S_{21}|$ were compared by means of a filter example that consists of two USFITs on quartz. Both the curves agree well. They are characterized by a dip in the passband and a strong ripple in the upper transition band and upper stopband. These features are a consequence of diffraction, as shown by an analysis neglecting diffraction. The analysis method can also be applied for SPUDT filters.

References

[1] A. P. van den Heuvel, "Use of rotated electrodes for amplitude weighting in interdigital transducers," *Appl. Phys. Lett.*, vol. 21, pp. 280–282, Sept. 1972.
[2] C. K. Campbell, Y. Ye, and J. J. S. Papa, "Wide-band linear phase SAW filter design using slanted transducer fingers," *IEEE Trans. Sonics Ultrason.*, vol. SU-29, pp. 224–228, July 1982.
[3] L. P. Solie, H. P. Fredrickson, S. Lins, and C. Nelson, "A SAW filter bank using hyperbolically tapered transducers," in *Proc. IEEE Ultrason. Symp.*, 1988, pp. 83–86.
[4] J. Lamperski, "SAW filters with weighted tapered interdigital transducers," in *Proc. IEEE Ultrason. Symp.*, 1992, pp. 203–206.
[5] E. V. Bausk and I. B. Yakovkin, "Withdrawal weighted fan-shaped SAW transducers," *IEEE Trans. Ultrason., Ferroelect., Freq. Contr.*, vol. 42, pp. 164–167, Mar. 1995.
[6] H. Yatsuda, "Design techniques for SAW filters using slanted finger interdigital transducers," *IEEE Trans. Ultrason., Ferroelect., Freq. Contr.*, vol. 44, pp. 453–459, Mar. 1997.
[7] H. Yatsuda and K. Yamanouchi, "Automatic computer-aided design of slanted finger SAW filters using a building-block method," in *Proc. IEEE Ultrason. Symp.*, 1998, pp. 239–242.
[8] H. Yatsuda, "Design technique for nonlinear phase SAW filters using slanted finger interdigital transducers," *IEEE Trans. Ultrason., Ferroelect., Freq. Contr.*, vol. 45, pp. 41–47, Jan. 1998.
[9] C. B. Saw and C. K. Campbell, "Improved design of single-phase unidirectional transducers for low-loss SAW filter," in *Proc. IEEE Ultrason. Symp.*, 1987, pp. 169–172.
[10] L. Solie, "Tapered transducers—Design and applications," in *Proc. IEEE Ultrason. Symp.*, 1998, pp. 27–37.
[11] V. B. Chvets, P. G. Ivanov, V. M. Makarov, and V. S. Orlov, "Low-loss slanted SAW filters with low shape factors," in *Proc. IEEE Ultrason. Symp.*, 1999, pp. 51–54.
[12] E. M. Garber, D. S. Yip, and D. K. Henderson, "Design of high selectivity DART SPUDT's on quartz and lithium tantalate," in *Proc. IEEE Ultrason. Symp.*, 1994, pp. 7–12.
[13] G. Martin, R. Kunze, M. Weihnacht, and B. Wall, "A discrete one component wave model and its application to SAW resonator filters," *IEEE Trans. Ultrason., Ferroelect., Freq. Contr.*, vol. 41, pp. 503–511, July 1994.
[14] D. P. Morgan, *Surface-Wave Devices for Signal Processing*. Amsterdam, The Netherlands: Elsevier, 1985, pp. 133–134.

Guenter Martin was born in Dresden, Germany, on February 14, 1943. He received the Diploma degree in physics and the Ph.D. degree from the Technical University of Dresden, Dresden, Germany, in 1968 and 1973, respectively. His doctoral research concerned high-pressure investigations of ferroelectrics at low temperatures.

Since 1972, he has been a Scientific Researcher at the Institute for Solid State and Materials Research Dresden, Dresden, Germany. His activities have been directed to solid-state acoustics, ferroelectric ceramics, and SAWs. He is currently involved with modeling and new solutions of SAW devices.

Dongpei Chen (M'96) received the B.S. degree from the University of Science and Technology of China (USTC), Beijing, China, in 1965.

From 1965 to 1975, he was a faculty member in the Department of Radio and Electronics, USTC. From 1976 to 1990, he was with the Institute of Acoustics, Chinese Academy of Sciences, as a Research Associate and then a Professor, where he was involved with the analyses of SAW propagating and scattering, SAW devices, SAW-based analog signal processing, and acoustooptic interaction. From 1982 to 1984, he was a Visiting Scientist with Research Laboratory of Electronics (RLE), the Massachusetts Institute of Technology (MIT), Cambridge. From 1991 to 1995, he was with Advanced SAW Products (ASP), Bevaix, Switzerland. Since 1996, he has been with Vectron International, Hudson, NH, where he is currently a Senior SAW Research and Development Engineer involved with modeling and design tool creating of various low-loss SAW filters and resonators.